Infrared Physics & Technology 55 (2012) 449–453

Contents lists available at SciVerse ScienceDirect

Infrared Physics & Technology

journal homepage: www.elsevier.com/locate/infrared

Phase resolved near-field imaging of propagating waves in infrared tapered slot antennas

Louis A. Florence [a], Edward C. Kinzel [b], Robert L. Olmon [c], James C. Ginn [d], Markus B. Raschke [c], Glenn D. Boreman [a,b,*]

[a] CREOL, The College of Optics & Photonics, University of Central Florida, 4000 Central Florida Blvd., Orlando, FL 32816, USA
[b] Department of Physics and Optical Science, University of North Carolina at Charlotte, 9201 University City Blvd., Charlotte, NC 28223, USA
[c] Department of Physics, University of Colorado, 390 UCB, Boulder, CO 80309, USA
[d] Plasmonics Inc., 12565 Research Pkwy, Suite 300, Orlando, FL 32826, USA

HIGHLIGHTS

- We use IR near-field microscopy to visualize modes on tapered slot antennas.
- We measure phase reversal across the slot and traveling waves on the antenna.
- Our technique allows near field-imaging of antennas of multi-wavelength dimension.

ARTICLE INFO

Article history:
Received 24 April 2012
Available online 27 July 2012

Keywords:
Tapered slot antenna
Infrared antenna
End fire antenna
Broadband antenna
Near field imaging

ABSTRACT

Tapered slot antennas (TSAs) consist of a planar non-resonant structure which couples incident radiation to a propagating waveguide mode. They are commonly used at microwave and radio frequencies because they are fundamentally broadband and have small profiles. Because of their planar layout and broadband response they have recently been scaled to infrared frequencies where they have advantages for sensing and energy harvesting. We use scattering-type scanning near-field optical microscopy (*s*-SNOM) to study the mode transformation of two types of TSA operating in the thermal infrared ($\lambda_0 = 10.6\ \mu m$) with respect to electric field amplitude and phase. The results agree well with simulation showing both the phase reversal across the tapered slot and the traveling of wave fronts along the tapered slot, yet they also reveal high sensitivity of device performance to inhomogeneities in the geometry or illumination. This study will aid future design and analysis of practical non-resonant antennas operating at optical and infrared frequencies.

1. Introduction

Advances in fabrication technology have enabled the development of antennas operating at optical and infrared wavelengths. These devices offer potential improvements for sensing [1–3], energy harvesting [4], diffractive optics [5], and non-linear optics [6]. Many of the designs and analytical techniques developed at radio and microwave frequencies can be scaled down to these shorter wavelengths. Both resonant [7,8] and traveling wave infrared antennas [9] have been demonstrated at infrared frequencies. While planar standing wave antennas such as dipoles [1,7,10–12] and Yagi-Uda [13] infrared antennas provide appreciable gain and directional radiation patterns, their bandwidth is fundamentally limited by resonance requirements.

Non-resonant antennas offer the potential for much broader bandwidth. The classical example is the horn antenna which permits an incident plane wave to gradually transform from a freely propagating mode to a confined mode in a waveguide. A tapered slot antenna (TSA) operates similarly but is two dimensional. This makes the TSA compatible with planer layer-by-layer manufacturing techniques, and it has found use at radio frequencies in printed circuit board packages [14]. These manufacturing considerations also make TSAs appealing for use at optical and infrared wavelengths where dimensional considerations require fabrication to be accomplished using IC thin-film techniques. In addition, the potential for large bandwidth makes TSAs potentially appealing for applications in sensing and energy harvesting.

There are several obstacles that are common to designing infrared antennas. The feature sizes scale with wavelength and are thus much smaller than their RF counterparts. For example, to ensure

* Corresponding author at: Department of Physics and Optical Science, University of North Carolina at Charlotte, 9201 University City Blvd., Charlotte, NC 28223, USA. Tel.: +1 704 687 8173; fax: +1 704 687 8197.
E-mail address: gboreman@uncc.edu (G.D. Boreman).

1350-4495/$ - see front matter © 2012 Elsevier B.V. All rights reserved.
http://dx.doi.org/10.1016/j.infrared.2012.07.008

confinement, the terminating slotline must be substantially smaller than the free-space wavelength, typically on the order of 500 nm for 10.6 μm radiation. Also, the material properties at optical and infrared wavelengths are generally less desirable than at longer wavelengths. At infrared wavelengths, metals exhibit dispersion and ohmic loss [15], and most oxide and polymer substrates have absorptive phonon modes. It is possible to overcome these challenges, but proper design requires deviation from the idealized analytic solutions developed for the microwave spectrum [16]. The lack of well defined analytic solutions requires full-wave numerical simulation, which in turn needs to be experimentally validated.

Interferometric homodyne scattering-type scanning near-field optical microscopy (*s*-SNOM) allows for the direct resolution of the amplitude and phase of the local electric field at nanometer length scales. Recently, this approach has been used to study isolated dipole antennas [10], coplanar striplines excited by dipole antennas [11,12], and Yagi-Uda antennas [13]. It has also been used to study metamaterial surfaces in the infrared [17,18] as well as propagating surface phonon waves [19].

In this paper we explore geometries for broadband mode transformation and combination at infrared frequencies through two different TSA designs. The electric field amplitude and phase distributions as measured by *s*-SNOM provide insight into the details of the mode transformation. We show that despite promising results from numerical models, the actual mode transformation is very sensitive to illumination conditions and fine geometric details governing the phase interaction on different parts of the structure. The accurate characterization of the fields around the TSA facilitates better targeted design of antennas with desired properties.

2. TSA design and fabrication

The TSA consists of two metal planes, either free standing or supported by a substrate, with a tapered slotline between the planes. These metal planes act as the outer edge of a waveguide, gradually confining coupled radiation into the slotline. Conventionally, the antenna is intended to operate in an endfire fashion, with radiation entering the aperture along the same axis as the slotline and exciting a quaid-TEM mode in the slotline [16]. In the infrared version of the TSA, the metal planes are not mechanically strong enough to be free standing and must be supported by a substrate. In this work the TSA is separated from a silicon substrate by a layer of benzocyclobutene (BCB). The BCB is added because it has a lower index than Si (n_{BCB} = 1.57 at 10.6 μm) and is an electrical insulator. The latter point is essential when a sensing element, such as a metal–oxide–metal (MOM) diode, is added to the slotline [1].

Unfortunately the use of a MOM diode prevents overcoating the TSA with a matching dielectric. Because the metal planes are not bounded by a uniform dielectric (as they would be in a conventional RF TSA) the behavior of the antenna is significantly modified. We previously showed that IR TSAs bounded with a BCB substrate and air superstrate have a maximum responsivitiy 30° above the endfire direction (60° from the surface normal) [9]. Because this behavior is a significant departure from established RF designs we choose to study it with *s*-SNOM.

Two different TSAs were designed and fabricated for this study and are shown in Fig. 1. The first device is a traditional linear tapered slot antenna (LTSA) (Fig. 1a) with a tapered slot cut from a rectangular metal plane. This antenna has been shown to work in the microwave region, and is expected to sustain surface waves on the metal and parallel plate modes on the sides [16]. The second is a V-shaped linear tapered slot antenna (V-LTSA) (Fig. 1b) similar to earlier designs built and characterized in [9]. The devices are

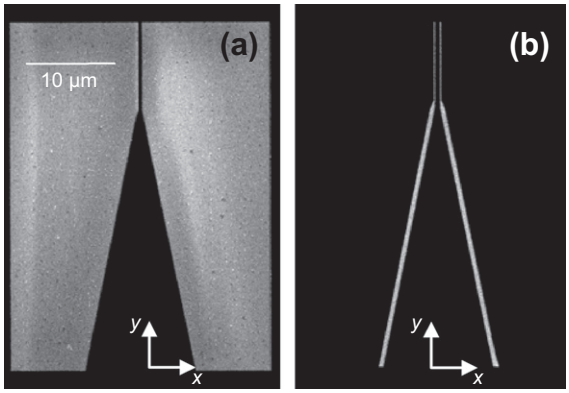

Fig. 1. SEM images of (a) the linear tapered slot antenna (LTSA) and (b) the V-shaped linear tapered slot antenna (V-LTSA).

built on 1.5 μm of BCB which is spin coated onto a [0 0 1] crystalline silicon wafer. The dimensions of the tapered slot are identical for both devices. The opening aperture is 12.5 μm across, and the length of the taper is 30 μm. The slotline is 10 μm long and 500 nm wide. The V-shaped antenna has 200 nm wide wires in the slotline, and 600 nm wide wires in the antenna arms in order to maintain the design of previously reported devices. The LTSA slotline is cut from a metal plane that is 29.5 μm wide. These patterns are written into an MMA/PMMA stack using an electron-beam lithography system. After depositing a 5 nm titanium adhesion layer, 60 nm of gold are deposited using a high-vacuum electron-beam evaporator. Residual resist is lifted off, leaving the gold antenna patterns on BCB.

It should be noted that these antennas differ from the design previously studied [9], since there is no detector or feedpoint in the slotline, and the BCB substrate extends in the endfire direction. Historically, the taper termination coincides with the edge of the substrate. Their length is shorter than previously reported devices in order to ensure that the device dimensions are on the same scale as the exciting radiation spot size (60 μm). Despite these discrepancies, wave propagation patterns and antenna response similar to the tested devices are expected. Slotlines of similar configuration and length have been shown to reduce the amplitude of the radiation by a factor of less than 1/e [20]; therefore, reflections from the open terminus of the slotline should not result in appreciable standing waves formed within the slotline.

3. Operation of the *s*-SNOM system

A schematic of the *s*-SNOM system is shown in Fig. 2. Our instrument design is similar to the *s*-SNOM used in [10,11,18]. The *s*-SNOM system uses an atomic force microscope (Bruker,

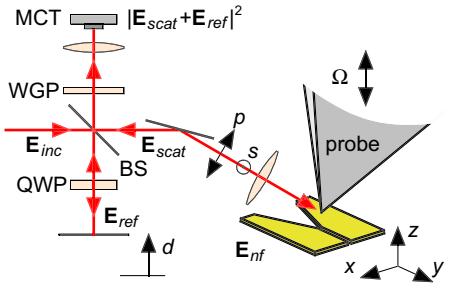

Fig. 2. Schematic of scattering-type scanning near-field optical microscope (*s*-SNOM). S-polarized light is incident on the antenna, and the scattered p-polarization light is collected.

INNOVA) operating in tapping mode. In this study we use an Arrow NCPt (Nanoworld) silicon AFM probe which is platinum coated in order to enhance the scattering of the near-field. The cantilever dithers at ~270 kHz with an amplitude of ~20 nm as the antenna is raster scanned beneath the tip. A closed loop control maintains a constant force interaction between the sample and tip during scanning. The tip is illuminated with an s-polarized (with respect to the sample) 10.6 μm CO_2 laser focused to an elliptical spot with a minor axis of 60 μm. The illumination strikes the sample with a $\theta = 60°$ angle of incidence relative to the surface normal which coincides with the maximum response direction for the TSA.

During scanning the TSA is excited by the incident laser beam. Energy couples to propagating waves along the antenna. This results in electric fields closely bound to the surface of the antenna. The probe interacts with these fields and scatters some of the energy back into propagating light. A portion of the tip-scattered light is collected by the same objective used to focus the incident laser beam and passes through a beam splitter. A wire-grid polarizer ensures that only the p-polarized light caused by scattering is collected and mixed with a reference signal. This cross-polarization selectivity reduces the signal caused by scattering events other than the tip. The resulting interference is recorded using a liquid nitrogen-cooled HgCdTe detector which is coupled to a lock-in amplifier operating at the second harmonic of the dithering frequency. Previous studies have shown that this configuration results in a signal that is closely correlated to the z-component (normal to the surface) of the electric field [10–14]. The signal is effectively proportional to

$$i \propto |E_{nf} + E_{ref}|^2 = |E_{nf}|^2 + E_{ref}|^2 E_{nf} \cdot E_{ref}| \cos\varphi \quad (1)$$

where $\varphi = \varphi_{nf} - d \cdot 4\pi/\lambda_0$, denoting the difference between the reference phase and the phase of the near-field electric field at the point in the sample directly beneath the probe. By adjusting the delay length d of the reference beam we can control the phase at which the electric field is sampled. We compile multiple images at different phases and perform a least-squares fit on a point-by-point basis to extract phase. This procedure results in recording only the portion of the field that varies with respect to the phase of the reference beam and thus accomplishes some of the background suppression that would be provided by dithering the reference mirror [19].Because the antenna extends several wavelengths and the sample must be translated over the entire length to image it, we observe a phase shift during scanning [21]. Initially, the antenna is excited at its entrance aperture (the x-axis in Fig. 1). As the antenna is scanned in the y-direction the phase of the incident light at the aperture shifts due to the off-normal excitation. If φ represents the actual phase, φ_0 represents the measured phase, y is the longitudinal distance scanned and $k_{0,y}$ is the free-space wave vector component in the longitudinal direction, the additional scanning phase can be accounted for in post-processing so that

$$\varphi = \varphi_0 - y \cdot k_{0,y} \quad (2a)$$

where

$$k_{0,y} = k_0 \sin\theta \quad (2b)$$

Here, θ is the angle between the antenna's surface normal and the incident radiation wave vector.

4. Results

Fig. 3 shows experimental results for the linear TSA (SEM image in Fig. 1a). We scanned the antenna seven times at increments of $\Delta\varphi = 45°$ ($\Delta d = 1.325$ μm). During the course of scanning, the s-SNOM simultaneously records AFM data, which is shown for one of the scans in Fig. 3a. Each image shows a 45×45 μm^2 scan field. Fig. 3b–d show data extracted from a least-squares fit of the raw s-SNOM data which removes some artifacts of self-homodyne interference. The amplitude plot (Fig. 3b) is normalized to the maximum signal over the scan. Fig. 3c shows the phase data as recorded by the s-SNOM. When this is corrected with Eq. (2) we obtain the image in Fig. 3d at a single phase. If this is animated over phase we clearly see waves propagating over the surface of the antenna in the $+y$ direction.

We modeled the antenna using a full-wave finite element method solver (HFSS, ANSYS Inc.). To increase simulation accuracy we included material properties acquired for the materials at 10.6 μm using spectral ellipsometery. We modeled the excitation as a Gaussian beam focused on the center of the entrance aperture (the origin in Figs. 1a and 3a). The amplitude of the z-component of the electric field 5 nm above the top surface of the antenna is

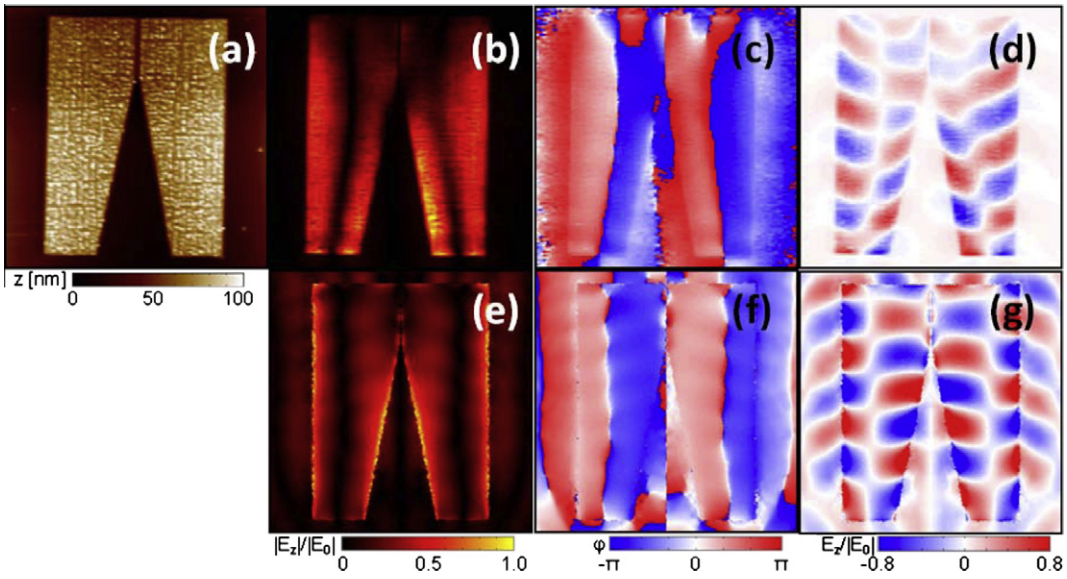

Fig. 3. Experimental s-SNOM results for LTSA compared to simulation (a) AFM acquired topography, (b) near-field amplitude, (c) near-field phase, (d) local field at $\varphi = 0°$ corrected for scanning, (e) simulated $|E_z|$ 5 nm above antenna, (f) phase of $|E_z|$ corrected for scanning and (g) $|E_z|$ at $\varphi = 0°$.

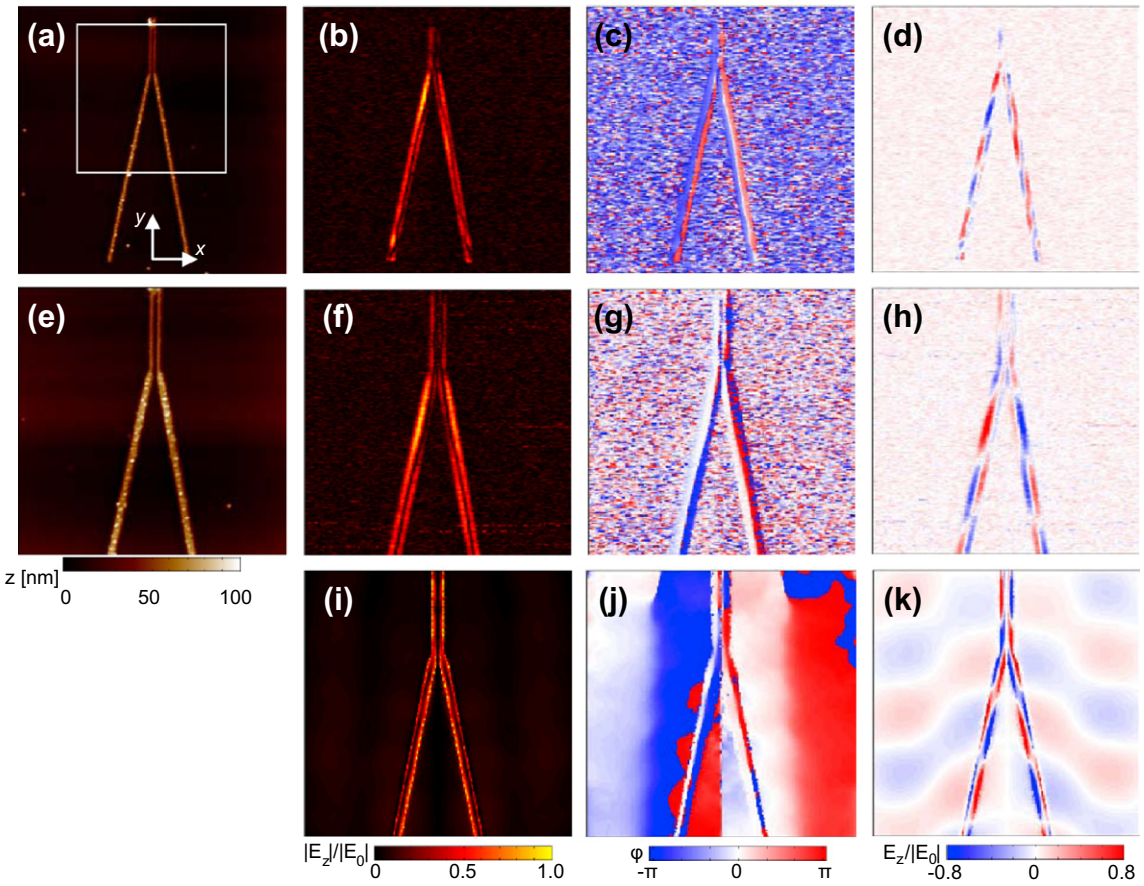

Fig. 4. Experimental *s*-SNOM results for V-LTSA compared to simulation (a and e) AFM acquired topography, (b and f) near-field amplitude, (c and g) near-field phase, (d and h) local field at $\varphi = 0°$ corrected for scanning, (i) simulated $|E_z|$ 5 nm above antenna, (j) phase of $|E_z|$ corrected for scanning and (k) $|E_z|$ at $\varphi = 0°$. Figs. (e–k) show a closer image of the area in (a).

plotted in Fig. 3e. This is normalized to the electric field of the incident field. Fig. 3f shows the phase map obtained from simulation after adding the scanning induced phase delay. Finally, Fig. 3g shows the field at a given phase angle without the simulation the scanning phase so that it corresponds directly to Fig. 3d.

We repeated both the *s*-SNOM experiment and the simulation for the V-LTSA. Simulation predicts that the response from this antenna (how much light is coupled into the slot portion of the waveguide) will be greater than the LTSA. In the V-LTSA, the single-wire waveguide modes are combined and transformed into coplanar strip transmission line modes as the antenna narrows [11,12]. The results for the V-LTSA are shown in Fig. 4. Because the features are finer for this antenna, a second set of images was taken closer to the entry point of the waveguide portion of the antenna. Fig. 4a–d and e–k shows $45 \times 45\ \mu m^2$ and $25 \times 25\ \mu m^2$ field-scans, respectively. The HFSS simulation is set-up identically to Fig. 3e–g, with the incident laser beam centered on the origin. The simulation of the V-LTSA predicts that there is minimal field away from the antenna structure. This agrees with the experiment. The minimal field away from the metal makes the resolution of the phase prone to error in this region. However, there is good phase agreement between the experiment and the simulation in regions above the antenna.

Figs. 3 and 4 show good qualitative agreement between simulation and experiment in both phase and amplitude. There are the same number of wave cycles along the inner edges of the TSA in each figure, and the linear null region that runs the length of both antennas is correctly predicted by simulation. The measured field magnitude in the slotline is less than predicted by simulation; we attribute this to attenuation of the field in the antenna. The phase interaction of the light on opposite sides of the waveguide may play a part in the increased attenuation. While the waveguide mode for the LTSA in the simulation (Fig. 3g) is asymmetric with respect to phase across the waveguide, the measurement (Fig. 3d) exhibits a substantial longitudinal field component, indicating that attainment of the proper phase for mode transformation at the constriction is very sensitive to illumination conditions and fine details of the geometry of the structure.

The measured near-field V-LTSA (Fig. 4h) agrees roughly with the numerical simulation (Fig. 4k). On the open end of the structure, the light is guided as two single-wire modes opposite in phase. At the constriction, the modes converge, forming a single dual-wire mode similar to that of a coplanar stripline. In this way, the V-LTSA can be considered a mode combiner. However, the combined mode in the slotline is attenuated more than expected, possibly due to the effects of scattering from the relatively rough edges of the antenna and slotline which are not accounted for in the HFSS model.

In both experiment and simulation the V-LTSA shows more pronounced fields in the terminated slotline portion of the antennas. However, this is not noticeably higher than the field at the entrance aperture suggesting that these antennas do not have a high confinement. Moreover, the difference in refractive index between the BCB substrate and the air superstrate cause the antenna to act as an inefficient leaky waveguide [16]. The losses inherent to the structure prevent any noticeable increase in field magnitude as

the signal progresses along the tapered region of the antenna, both in simulation and in actual measurement. Simulations of the structure with matching dielectric above the TSA (not shown) predict much better response as well as a peak of directivity in the endfire direction. However, it would not be possible to study these antennas directly with *s*-SNOM because the fields would be confined within the dielectric.

We note that the *s*-SNOM technique provides fine structure measurement of spatially transient fields, allowing high spatial resolution in the resulting images. This high spatial resolution allows us to visualize the mode transformation occurring along the taper into the slotline. Additionally, the high resolution of the image allows point by point comparison to simulation, allowing validation of design parameters. The simulation results are for a beam centered on the entrance aperture. The fact that the experiment agrees with this result indicates that the coupling occurs at this entrance aperture for the physical antenna. That is, we would expect discrepancies if the coupling was distributed over the length of the antenna. The simulation predicts greater fields in the area surrounding the antenna than are observed experimentally. This indicates that probe is more efficient scattering the field when it is directly above the metal antenna. This agrees with analytic models [22] of the *s*-SNOM process that model the antenna as an image plane for the probe.

5. Conclusion

We have shown that the near fields of a non-resonant tapered slot antennas of multi-wavelength dimensions can be accurately imaged using a scattering *s*-SNOM system. The resulting images show high spatial resolution, allowing for accurate magnitude and phase imaging for fine features. These results are in good agreement with numerical simulation. This serves to validate numerical models of the structure as well as the correspondence of the normal component of near-surface electric field to the *s*-SNOM signal, but it highlights the differences between ideal structures and actual ones, where the device behavior can be very sensitive to illumination conditions and fine geometrical details. Future work to improve infrared TSAs should focus on improving coupling efficiency. This will increase the magnitude of the near-fields in the terminating slotline, allowing for improved sensing. In order to increase the coupling efficiency, the antenna needs to be placed between a substrate and a superstrate that have similar indices of refraction. One method of doing this is reducing the index of the substrate by using a substance such as aerogel. The other method is using a higher index superstrate to coat the antenna.

References

[1] J.A. Bean, A. Weeks, G.D. Boreman, Performance optimization of antenna-coupled Al/AlO_x/Pt tunnel diode infrared detectors, IEEE J. Quant. Electron. 47 (2011) 126–135.
[2] L. Tang, S.E. Kocabas, S. Latif, A.K. Okyay, D.-S. Ly-Gagnon, K.C. Saraswat, D.A.B. Miller, Nanometre-scale germanium photodetector enhanced by a near-infrared dipole antenna, Nat. Photon. 2 (2008) 226–229.
[3] I. Wilke, W. Herrmann, Integrated nanostrip dipole antennas for coherent 30 THz infrared radiation, Appl. Phys. B 95 (1994) 87–95.
[4] R. Corkish, M.A. Green, T. Puzzer, Solar energy collection by antennas, Solar Energy 73 (2002) 395–401.
[5] J. Ginn, B. Lail, J. Alda, G. Boreman, Planar infrared binary phase reflectarray, Opt. Lett. 33 (2008) 779–781.
[6] D.A. Genov, A.K. Sarychev, V.M. Shalaev, A. Wei, Resonant field enhancements from metal nanoparticle arrays, Nano Lett. 4 (2004) 153–158.
[7] J. Alda, J.M. Rico-Garcia, J.M. Lopez-Alonso, G. Boreman, Optical antennas for nano-photonic applications, Nanotechnology 16 (2005) 230–234.
[8] F. Neubrech, D. Weber, R. Lovrincic, A. Pucci, M. Lopes, T. Toury, M. Lamy de La Chapelle, Resonances of individual lithographic gold nanowires in the infrared, Appl. Phys. Lett. 9 (3) (2008) 163105.
[9] L.A. Florence, B.A. Slovick, E.C. Kinzel, J.A. Bean, G.D. Boreman, Infrared linear tapered slot antenna, IEEE Antennas Wireless Propagation Lett. 10 (2011) 1299–1301.
[10] R.L. Olmon, P.M. Krenz, A.C. Jones, G.D. Boreman, M.B. Raschke, Near-field imaging of optical antenna modes in the mid-infrared, Opt. Exp. 16 (2008) 20295–20305.
[11] P.M. Krenz, R.L. Olmon, B.A. Lail, M.B. Raschke, G.D. Boreman, Near-field measurement of infrared coplanar strip transmission line attenuation and propagation constants, Opt. Exp. 18 (2010) 21678–21686.
[12] M. Schnell, P. Alonso-Gonzalez, L. Arzubiaga, F. Cananova, L.E. Hueso, A. Chuvillin, R. Hillenbrand, Nanofocusing of mid-infrared energy with tapered transmission lines, Nat. Photon. 5 (2011) 283–287.
[13] J. Dorfmüller, D. Dregely, M. Esslinger, W. Khusin, R. Vogelgesang, K. Kern, G. Giessen, Near-field dynamics of optical Yagi-Uda nanoantennas, Nano Lett. 11 (2011) 2819–2824.
[14] I.K. Kim, N. Kidera, S. Pinel, J. Papapolymerou, J. Laskar, J. Yook, M. Tentzeris, Linear tapered cavity-backed slot antenna for millimeter-wave LTCC modules, IEEE Antennas Wireless Propagation Lett. 5 (2006) 175–178.
[15] F. Gonzalez, J. Alda, J. Simon, J. Ginn, G. Boreman, The effect of metal dispersion on the resonance of antennas at infrared frequencies, Infrared Phys. Technol. 52 (2009) 48–51.
[16] R.Q. Lee, R.N. Simons, Tapered slot antennas, in: K.F. Lee, W. Chen (Eds.), Advances in Microstrip and Printed Antennas, Wiley & Sons, New York, 1997, p. 444.
[17] T. Zentgraf, J. Dorfmüller, C. Rockstuhl, C. Etrich, R. Vogelgasang, K. Kern, T. Pertsch, F. Lederer, H. Giessen, Amplitude- and phase-resolved optical near-fields of split-ring-resonator-based metamaterials, Opt. Lett. 33 (2008) 848–850.
[18] E. Kinzel, J. Ginn, R. Olmon, D. Shelton, B. Lail, I. Brenner, M. Sinclair, M. Raschke, G. Boreman, Phase resolved near-field mode imaging for the design of frequency-selective surfaces, Opt. Exp. 20 (2012) 11986–11993.
[19] A. Huber, N. Ocelic, D. Kazantsev, R. Hillenbrand, Near-field imaging of mid-infrared surface phonon propagation, Appl. Phys. Lett. 8 (7) (2005) 081103.
[20] T. Mandviwala, B. Lail, G. Boreman, Characterization of microstrip transmission lines at IR frequencies – modeling, fabrication and measurements, Microwave Optical Technol. Lett. 50 (2008) 1232–1237.
[21] N. Ocelic, A. Huber, R. Hillenbrand, Pseudoheterodyne detection for background-free near-field spectroscopy, Appl. Phys. Lett. 8 (9) (2006) 101124.
[22] F. Keilmann, R. Hillenbrand, Near-field microscopy by elastic light scattering from a tip, Philos. Trans. R. Soc. Lond. A 362 (2004) 787–805.